Supporting Information

Classical Magnetic Dipole Moments for the Simulation of Vibrational Circular Dichroism by *ab initio* Molecular Dynamics

Martin Thomas Barbara Kirchner

Mulliken Center for Theoretical Chemistry, Rheinische Friedrich-Wilhelms-Universität Bonn, Beringstraße 4, 53115 Bonn, Germany.
E-mail: martin.thomas@uni-bonn.de, kirchner@thch.uni-bonn.de

1 Computational Details

In order to assess the performance of our approach, we performed AIMD simulations of several chiral molecules. In particular, we studied a single 2-butanol molecule as well as bulk phase systems of 2-butanol, propylene oxide, and α-pinene (see also table S1). For liquid 2-butanol, we ran independent simulations of the two enantiomers to show that our method produces mirror symmetric spectra as this is a basic property of VCD.

The AIMD simulations were carried out using the CP2K program package.[1,2] Density functional theory with the BLYP exchange-correlation functional[3,4] and Grimme's dispersion correction D3[5] was employed as electronic structure method. The molecularly optimized double-zeta basis set (MOLOPT-DZVP-SR-GTH)[6] and Goedecker–Teter–Hutter pseudopotentials[7–9] were applied to all atoms with a plane wave cutoff of 280 Ry. A timestep of 0.5 fs was chosen, and the temperature was adjusted by a Nosé–Hoover thermostat chain[10–12] with a coupling time constant of 50 fs. The electron density was saved in Gaussian cube format with a stride of 1 in each simulation step. Classical molecular dynamics simulations for pre-equilibration were carried out with Lammps,[13] employing parameters from the general Amber force field[14] and atomic partial charges derived from a restrained electrostatic potential fit.[15]

The spectra were evaluated using Travis,[16–19] where we have implemented the methodology to calculate magnetic dipole moments and VCD intensities. In the main text, the following partial differential equation is derived:

$$\frac{\partial \rho(\mathbf{r},t)}{\partial t} = \boldsymbol{\nabla}\rho(\mathbf{r},t) \cdot \boldsymbol{\nabla}\alpha(\mathbf{r},t) + \rho(\mathbf{r},t)\Delta\alpha(\mathbf{r},t). \tag{1}$$

This equation is discretized on a regular grid by a finite difference method, so it is replaced by a system of linear equations. If the electron density is saved in Gaussian cube format, a

	(*R*)-2-Butanol (gas)	(*R*)-2-Butanol (liquid) (*S*)-2-Butanol (liquid)
Composition	1 C_4H_9OH	16 C_4H_9OH
Cell size (pm)	1200.0	1345.0
Density (g/cm^3)	–	0.81
Average temperature (K)	400	400
Equilibration time (ps)	5.0	10.0
Physical time (ps)	30.0	30.0
	(*R*)-Propylene oxide	(1*R*, 5*R*)-α-pinene
Composition	16 C_3H_6O	16 $C_{10}H_{16}$
Cell size (pm)	1230.0	1615.0
Density (g/cm^3)	0.83	0.86
Average temperature (K)	400	350
Equilibration time (ps)	10.0	5.0
Physical time (ps)	30.0	30.0

Table S1: Simulation parameters.

regular grid is already given by the input data. The time derivative and the gradient of the electron density are calculated by second-order central finite differences, so their values are known on the same grid. In a similar manner, the derivatives of the scalar field $\alpha(\mathbf{r}, t)$ are approximated by second-order central finite differences. If the grid consists of $n_x \times n_y \times n_z$ points with spacings of h_x, h_y, and h_z along the three axes, this leads to

$$(D_x\alpha)_{i,j,k} = \frac{\alpha_{i+1,j,k} - \alpha_{i-1,j,k}}{2h_x}, \tag{2}$$

$$(D_y\alpha)_{i,j,k} = \frac{\alpha_{i,j+1,k} - \alpha_{i,j-1,k}}{2h_y}, \tag{3}$$

$$(D_z\alpha)_{i,j,k} = \frac{\alpha_{i,j,k+1} - \alpha_{i,j,k-1}}{2h_z} \tag{4}$$

for the components of the gradient and to

$$\begin{aligned}(L\alpha)_{i,j,k} = {} & \frac{\alpha_{i+1,j,k} - 2\alpha_{i,j,k} + \alpha_{i-1,j,k}}{h_x^2} + \frac{\alpha_{i,j+1,k} - 2\alpha_{i,j,k} + \alpha_{i,j-1,k}}{h_y^2} \\ & + \frac{\alpha_{i,j,k+1} - 2\alpha_{i,j,k} + \alpha_{i,j,k-1}}{h_z^2}\end{aligned} \tag{5}$$

for the Laplacian, where i, j, and k number the points along the x, y, and z axes, respectively. The periodic boundary conditions are taken into account by $i \in \mathbb{Z}/n_x\mathbb{Z}$, $j \in \mathbb{Z}/n_y\mathbb{Z}$, and $k \in \mathbb{Z}/n_z\mathbb{Z}$, so, *e. g.*, the successor of $i = n_x - 1$ is $i = 0$ and the predecessor of $i = 0$ is $i = n_x - 1$. The grid is linearized in such a way that x lines and then xy planes of the grid follow one after another, so $l = i + jn_x + kn_xn_y$ becomes the new index in the one-dimensional

arrays. This leads to the following matrix representation of the system of linear equations:

$$\mathbf{A}\begin{pmatrix} \alpha_0 \\ \vdots \\ \alpha_{n_x n_y n_z - 1} \end{pmatrix} = \begin{pmatrix} \left(\frac{\partial \rho}{\partial t}\right)_0 \\ \vdots \\ \left(\frac{\partial \rho}{\partial t}\right)_{n_x n_y n_z - 1} \end{pmatrix}, \tag{6}$$

where $\mathbf{A} = \mathbf{B} + \mathbf{G} \in \mathbb{R}^{n_x n_y n_z \times n_x n_y n_z}$ with the definitions

$$\mathbf{B} = \begin{pmatrix} \mathbf{C}_0 & \mathbf{F}_0 & \mathbf{0} & & \mathbf{F}_0 \\ \mathbf{F}_1 & \mathbf{C}_1 & \mathbf{F}_1 & \ddots & \\ \mathbf{0} & \mathbf{F}_2 & \mathbf{C}_2 & \ddots & \mathbf{0} \\ & \ddots & \ddots & \ddots & \mathbf{F}_{n_z-2} \\ \mathbf{F}_{n_z-1} & & \mathbf{0} & \mathbf{F}_{n_z-1} & \mathbf{C}_{n_z-1} \end{pmatrix} \in \mathbb{R}^{n_x n_y n_z \times n_x n_y n_z}, \tag{7}$$

$$\mathbf{C}_m = \begin{pmatrix} \mathbf{D}_{mn_y} & \mathbf{E}_{mn_y} & \mathbf{0} & & \mathbf{E}_{mn_y} \\ \mathbf{E}_{mn_y+1} & \mathbf{D}_{mn_y+1} & \mathbf{E}_{mn_y+1} & \ddots & \\ \mathbf{0} & \mathbf{E}_{mn_y+2} & \mathbf{D}_{mn_y+2} & \ddots & \mathbf{0} \\ & \ddots & \ddots & \ddots & \mathbf{E}_{mn_y+n_y-2} \\ \mathbf{E}_{mn_y+n_y-1} & & \mathbf{0} & \mathbf{E}_{mn_y+n_y-1} & \mathbf{D}_{mn_y+n_y-1} \end{pmatrix} \in \mathbb{R}^{n_x n_y \times n_x n_y}, \tag{8}$$

$$\mathbf{D}_n = \begin{pmatrix} -2h_2\rho_{nn_x} & \frac{\rho_{nn_x}}{h_x^2} & 0 & & \frac{\rho_{nn_x}}{h_x^2} \\ \frac{\rho_{nn_x+1}}{h_x^2} & -2h_2\rho_{nn_x+1} & \frac{\rho_{nn_x+1}}{h_x^2} & \ddots & \\ 0 & \frac{\rho_{nn_x+2}}{h_x^2} & -2h_2\rho_{nn_x+2} & \ddots & 0 \\ & \ddots & \ddots & \ddots & \frac{\rho_{nn_x+n_x-2}}{h_x^2} \\ \frac{\rho_{nn_x+n_x-1}}{h_x^2} & & 0 & \frac{\rho_{nn_x+n_x-1}}{h_x^2} & -2h_2\rho_{nn_x+n_x-1} \end{pmatrix} \in \mathbb{R}^{n_x \times n_x}, \tag{9}$$

$$h_2 = \frac{1}{h_x^2} + \frac{1}{h_y^2} + \frac{1}{h_z^2}, \tag{10}$$

$$\mathbf{E}_n = \begin{pmatrix} \frac{\rho_{nn_x}}{h_y^2} & 0 & \cdots & 0 \\ 0 & \frac{\rho_{nn_x+1}}{h_y^2} & \ddots & \vdots \\ \vdots & \ddots & \ddots & 0 \\ 0 & \cdots & 0 & \frac{\rho_{nn_x+n_x-1}}{h_y^2} \end{pmatrix} \in \mathbb{R}^{n_x \times n_x}, \tag{11}$$

$$\mathbf{F}_m = \begin{pmatrix} \frac{\rho_{mn_x n_y}}{h_z^2} & 0 & \cdots & 0 \\ 0 & \frac{\rho_{mn_x n_y+1}}{h_z^2} & \ddots & \vdots \\ \vdots & \ddots & \ddots & 0 \\ 0 & \cdots & 0 & \frac{\rho_{mn_x n_y+n_x n_y-1}}{h_z^2} \end{pmatrix} \in \mathbb{R}^{n_x n_y \times n_x n_y}, \tag{12}$$

$$\mathbf{G} = \begin{pmatrix} \mathbf{H}_0 & \mathbf{K}_0 & \mathbf{0} & & -\mathbf{K}_0 \\ -\mathbf{K}_1 & \mathbf{H}_1 & \mathbf{K}_1 & \ddots & \\ \mathbf{0} & -\mathbf{K}_2 & \mathbf{H}_2 & \ddots & \mathbf{0} \\ & \ddots & \ddots & \ddots & \mathbf{K}_{n_z-2} \\ \mathbf{K}_{n_z-1} & & \mathbf{0} & -\mathbf{K}_{n_z-1} & \mathbf{H}_{n_z-1} \end{pmatrix} \in \mathbb{R}^{n_x n_y n_z \times n_x n_y n_z}, \tag{13}$$

$$\mathbf{H}_m = \begin{pmatrix} \mathbf{I}_{mn_y} & \mathbf{J}_{mn_y} & \mathbf{0} & & -\mathbf{J}_{mn_y} \\ -\mathbf{J}_{mn_y+1} & \mathbf{I}_{mn_y+1} & \mathbf{J}_{mn_y+1} & \ddots & \\ \mathbf{0} & -\mathbf{J}_{mn_y+2} & \mathbf{I}_{mn_y+2} & \ddots & \mathbf{0} \\ & \ddots & \ddots & \ddots & \mathbf{J}_{mn_y+n_y-2} \\ \mathbf{J}_{mn_y+n_y-1} & & \mathbf{0} & -\mathbf{J}_{mn_y+n_y-1} & \mathbf{I}_{mn_y+n_y-1} \end{pmatrix} \in \mathbb{R}^{n_x n_y \times n_x n_y}, \tag{14}$$

$$\mathbf{I}_n = \begin{pmatrix} 0 & \frac{\left(\frac{\partial \rho}{\partial x}\right)_{nn_x}}{2h_x} & 0 & & -\frac{\left(\frac{\partial \rho}{\partial x}\right)_{nn_x}}{2h_x} \\ -\frac{\left(\frac{\partial \rho}{\partial x}\right)_{nn_x+1}}{2h_x} & 0 & \frac{\left(\frac{\partial \rho}{\partial x}\right)_{nn_x+1}}{2h_x} & \ddots & \\ 0 & -\frac{\left(\frac{\partial \rho}{\partial x}\right)_{nn_x+2}}{2h_x} & 0 & \ddots & 0 \\ & \ddots & \ddots & \ddots & \frac{\left(\frac{\partial \rho}{\partial x}\right)_{nn_x+n_x-2}}{2h_x} \\ \frac{\left(\frac{\partial \rho}{\partial x}\right)_{nn_x+n_x-1}}{2h_x} & & 0 & -\frac{\left(\frac{\partial \rho}{\partial x}\right)_{nn_x+n_x-1}}{2h_x} & 0 \end{pmatrix} \in \mathbb{R}^{n_x \times n_x}, \tag{15}$$

$$\mathbf{J}_n = \begin{pmatrix} \frac{\left(\frac{\partial \rho}{\partial y}\right)_{nn_x}}{2h_y} & 0 & \cdots & 0 \\ 0 & \frac{\left(\frac{\partial \rho}{\partial y}\right)_{nn_x+1}}{2h_y} & \ddots & \vdots \\ \vdots & \ddots & \ddots & 0 \\ 0 & \cdots & 0 & \frac{\left(\frac{\partial \rho}{\partial y}\right)_{nn_x+n_x-1}}{2h_y} \end{pmatrix} \in \mathbb{R}^{n_x \times n_x}, \tag{16}$$

$$\mathbf{K}_m = \begin{pmatrix} \frac{\left(\frac{\partial \rho}{\partial z}\right)_{mn_x n_y}}{2h_z} & 0 & \cdots & 0 \\ 0 & \frac{\left(\frac{\partial \rho}{\partial z}\right)_{mn_x n_y+1}}{2h_z} & \ddots & \vdots \\ \vdots & \ddots & \ddots & 0 \\ 0 & \cdots & 0 & \frac{\left(\frac{\partial \rho}{\partial z}\right)_{mn_x n_y+n_x n_y-1}}{2h_z} \end{pmatrix} \in \mathbb{R}^{n_x n_y \times n_x n_y}. \tag{17}$$

For the BiCGstab(l) algorithm, we have adapted the FORTRAN code from reference 20. The convergence is improved by employing an incomplete LU factorization for preconditioning.[21] For memory efficiency, the compressed row storage format is used to store the matrices.[22] The convergence threshold for the BiCGstab(l) iterations is chosen in the following way: In the first simulation step, the solution guess for $\alpha(\mathbf{r}, t)$ is set to zero on the whole grid and the residual is computed. The threshold for all steps is selected relative to this residual. A relative convergence criterion of $1 \cdot 10^{-2}$ proves to be sufficient to converge the molecular magnetic

dipole moments within a few percent (see below). In order to improve the stability of the solution algorithm in a gas phase simulation where large regions of the cell are empty, it is possible to add a background electron density in the order of $10^{-2}\,e/\mathrm{nm}^3$. As shown below, this does not significantly distort the magnetic dipole moment.

Saving the electron density in each simulation step yields huge amounts of data. The complete electron density along the α-pinene trajectory in Gaussian cube format would, *e. g.*, occupy about 4.2 TB of disk space. Since the handling of such files is still not a routine task on modern computer systems, we have implemented a streaming scheme where TRAVIS runs at the same time as the AIMD simulation, directly consumes the Gaussian cube files written by CP2K, and just saves the molecular moments. This requires that the differential equation (1) is solved on the fly and, thus, it is a limiting factor for the speed of the AIMD simulation. At the moment, the code in TRAVIS is strictly serial, but we were still able to run CP2K in parallel on 16 cores while TRAVIS could keep up in processing the electron density. A more detailed analysis of the scaling behavior of the solution algorithm is necessary in the future, but these numbers show that the solution of the differential equation (1) provides only a minor contribution to the computational requirements for the simulation of VCD spectra when system sizes as in this work are investigated.

2 Convergence of the Molecular Magnetic Dipole Moments

Several parameters enter the numerical solution of the partial differential equation (1). In this section, we show that the molecular magnetic dipole moments are reasonably converged with respect to the timestep at which the electron density has to be sampled, the convergence threshold in the BiCGstab(l) algorithm, and the background electron density for gas phase simulations.

The timestep of the simulation has to be sufficiently small to allow to approximate the time derivative of the electron density well. For that reason, we performed a short simulation of the single 2-butanol molecule with a timestep of 0.1 fs and saved the electron density in all steps. At first, the magnetic dipole moment was calculated in each step by evaluating the whole trajectory. Afterwards, only every fifth snapshot and every tenth snapshot of the trajectory were processed, so the time derivative was computed with step sizes of 0.5 fs and 1.0 fs. The comparison of the resulting magnetic dipole moment vectors (see figure S1) shows that the difference between 0.1 fs and 0.5 fs is in the order of $10^{-5}\,\mu_\mathrm{B}$, which corresponds to a relative error of about 1 % here. For a step size of 1.0 fs, the deviation to 0.1 fs reaches the order of $10^{-4}\,\mu_\mathrm{B}$, corresponding to a relative error of about 5 %. This result indicates that a timestep of 0.5 fs is sufficient for the AIMD simulation if the electron density is processed in every step. Smaller timesteps do not significantly improve the magnetic dipole moment.

The selection of the convergence threshold in the BiCGstab(l) algorithm was described above. Three different values of the relative convergence criterion are compared in figure S2. The value

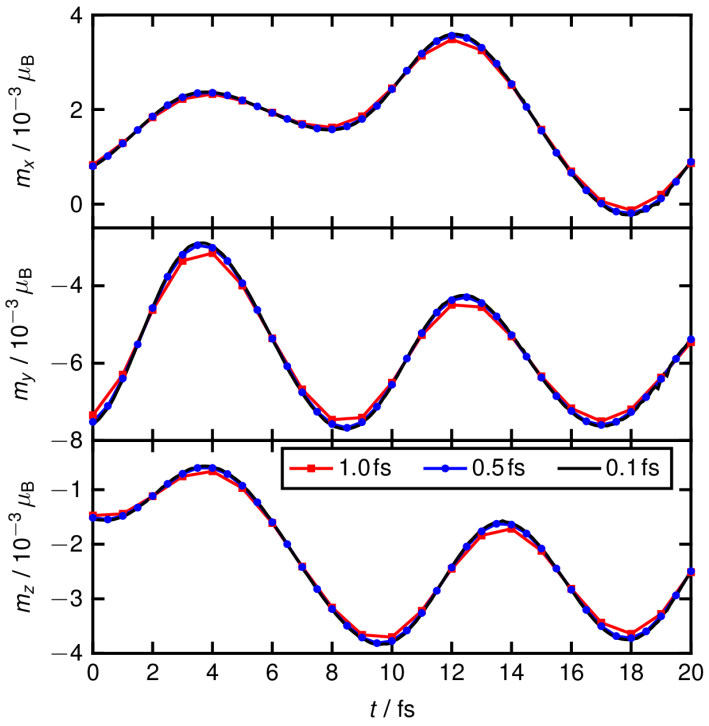

Figure S1: Vector components of the magnetic dipole moment of (*R*)-2-butanol for different timesteps.

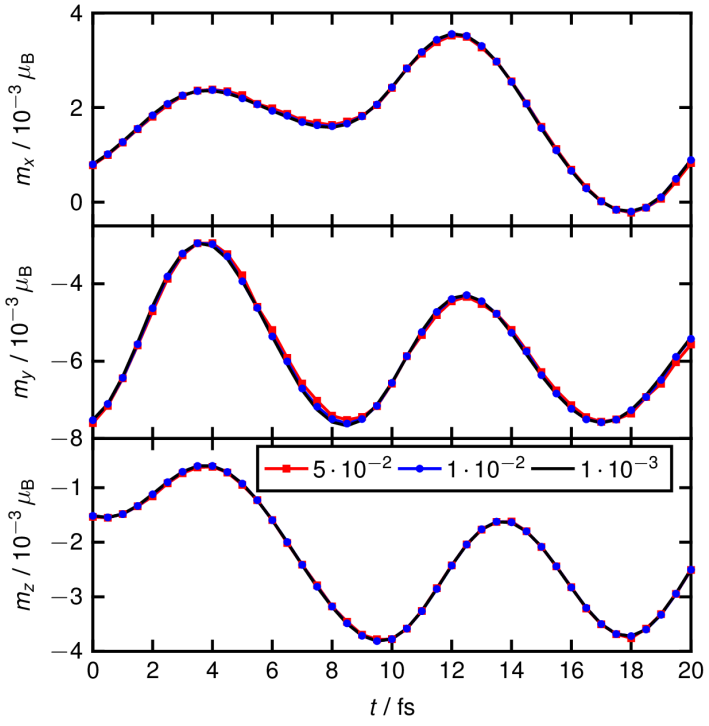

Figure S2: Vector components of the magnetic dipole moment of (*R*)-2-butanol for different convergence thresholds in the BiCGstab(l) algorithm.

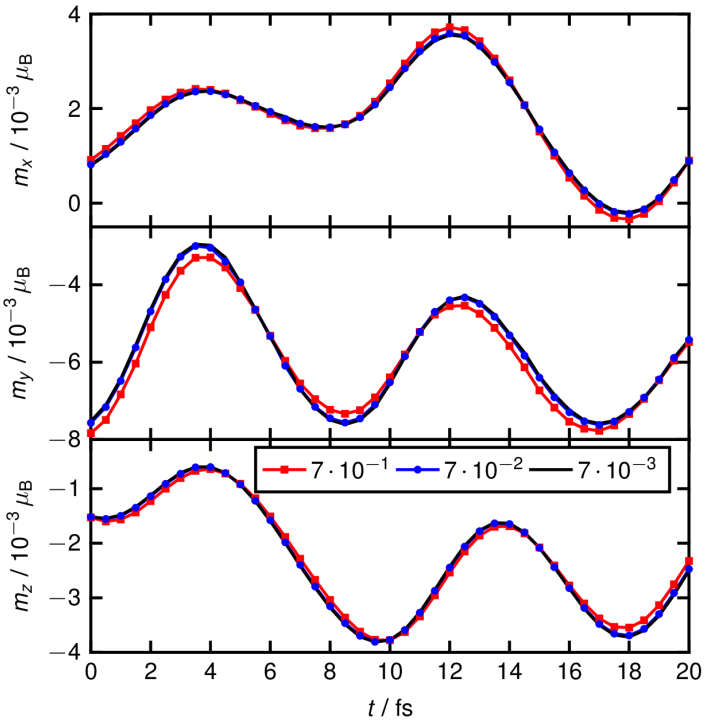

Figure S3: Vector components of the magnetic dipole moment of (*R*)-2-butanol for different values of the background electron density.

of $1 \cdot 10^{-3}$ is very tight, since in some snapshots, the algorithm is not able to completely reach this value. However, it is obvious that less tight criteria are sufficient to reasonably converge the magnetic dipole moment. Even with $5 \cdot 10^{-2}$, the relative deviations are in the order of a few percent, and a value of $1 \cdot 10^{-2}$ appears to be a proper choice.

An important issue while solving equation (1) are large empty regions in the simulation cell. At points where the electron density and its gradient vanish, the scalar field $\alpha(\mathbf{r}, t)$ can take arbitrary values without violating the equation. This strongly hampers the convergence of the solution algorithm, and for the 2-butanol molecule, it is impossible to obtain a reasonable result in any snapshot of the trajectory. In order to avoid this problem, a small constant background electron density was added to the system. This allows a small electric current to flow everywhere in the simulation cell, making the solution of the partial differential equation much more stable. For 2-butanol, we found that a background electron density of at least $7 \cdot 10^{-3}\, e/\mathrm{nm}^3$ (equal to 10^{-6} in atomic units) is necessary to sufficiently stabilize the algorithm. Still, this value is by several orders of magnitude lower than the maximal electron density in the molecule. The negligible influence on the magnetic dipole moment is confirmed by a comparison of the result with two larger values of the background electron density (see figure S3). Clear effects start to be visible with a background electron density of $7 \cdot 10^{-1}\, e/\mathrm{nm}^3$. Since the result with $7 \cdot 10^{-2}\, e/\mathrm{nm}^3$ is almost equal to $7 \cdot 10^{-3}\, e/\mathrm{nm}^3$, it can be assumed that the magnetic

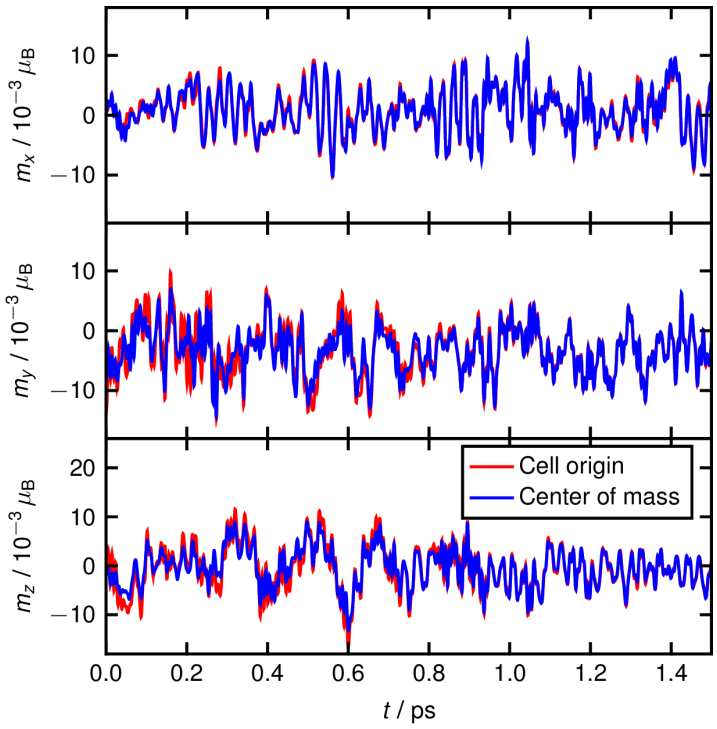

Figure S4: Vector components of the magnetic dipole moment of (*R*)-2-butanol for different choices of the reference point.

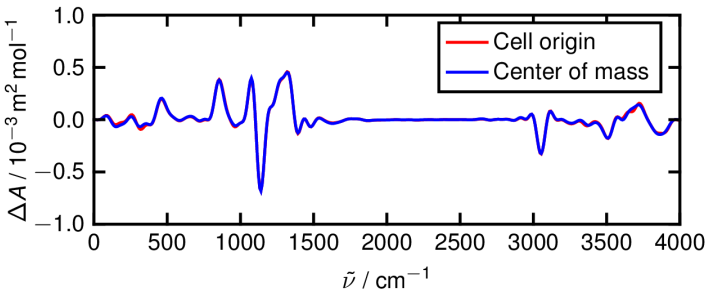

Figure S5: Simulated VCD spectra of (*R*)-2-butanol in the gas phase for different choices of the reference point for the magnetic dipole moment.

dipole moment is not affected by the latter in an unacceptable manner. It has to be noted that the background density is only needed for the gas phase simulation of 2-butanol. In all the bulk phase simulations carried out here, the unmodified electron density from the AIMD provides stable magnetic dipole moments.

3 Influence of the Reference Point

In order to investigate the influence of the reference point for the magnetic dipole moment on the VCD spectrum, we performed a short AIMD simulation (1.5 ps) of a single (*R*)-2-butanol

molecule with a timestep of 0.5 fs, and we calculated the magnetic dipole moments with the molecular center of mass and with the origin of the simulation cell as two different reference points. The comparison of these two choices (see figure S4) shows that the magnetic dipole moment is certainly dependent on the reference point, but the general oscillations due to the vibrations of the molecule are the same in both cases. Since just the time derivative of the magnetic dipole moment enters the expression for VCD, only minor differences are expected in the resulting spectra. This is confirmed by the spectra obtained from the small trajectory (see figure S5). Due to the much shorter trajectory length of 1.5 ps, these spectra are not converged as in the main text with a trajectory length of 30 ps, but it is clearly visible that the choice of the reference point for the magnetic dipole moment has only a minor influence on the VCD spectrum.

4 Further Applications

Besides 2-butanol, which is discussed in the main text, we studied also (*R*)-propylene oxide, which is one of the smallest chiral molecules in general. The IR and VCD spectra obtained from an AIMD simulation of 16 molecules are compared to experimental data[23–25] in figure S6. Furthermore, we performed a static calculation of the VCD spectrum of a single molecule using DALTON2016[26–28] with the BLYP exchange-correlation functional[3,4] and the def2-TZVP basis set.[29] The general agreement of simulation, static calculation, and experiment is very good. In the IR spectrum from the AIMD, only the intensity of the band at 782 cm^{-1} is overestimated and many fingerprint bands are slightly red-shifted again, but this is also in line with the shifts observed in an analysis of the Raman spectrum of propylene oxide by AIMD.[30] Several bands in the IR spectrum are merged, so the AIMD produces only two distinct peaks instead of four between 1300 cm^{-1} and 1550 cm^{-1}, and the splitting of the two signals around 1100 cm^{-1} is less pronounced. This effect is directly transferred to the VCD spectrum, where the simulated intensities of the negative–positive–negative band feature around 1100 cm^{-1} and the weak bands at 1458 cm^{-1} and 1499 cm^{-1} are lower than in the experiment. It should be noted that the peaks of shifted modes are just merged in the IR spectrum, while the intensities of peaks with opposite sign can cancel each other in the VCD spectrum. Thus the VCD spectrum is more sensitive to a shift of the wavenumbers by the underlying electronic structure method. The simulation also predicts a positive peak at 782 cm^{-1} with no counterpart in the experiment, but this is found in the same way in the static calculation, so it is not a particular issue of our VCD model in the AIMD. Most importantly, the intense experimental bands at 895 cm^{-1}, 950 cm^{-1}, and 1407 cm^{-1} are reproduced very well by the simulation.

Another example is the biomolecule (1*R*, 5*R*)-α-pinene. The IR and VCD spectra obtained from an AIMD simulation of 16 molecules are compared to experimental data[31,32] in figure S7. The IR spectrum of α-pinene possesses a lot of bands in the fingerprint region and it is difficult to find a fully unambiguous assignment between simulation and experiment due to the shifts of

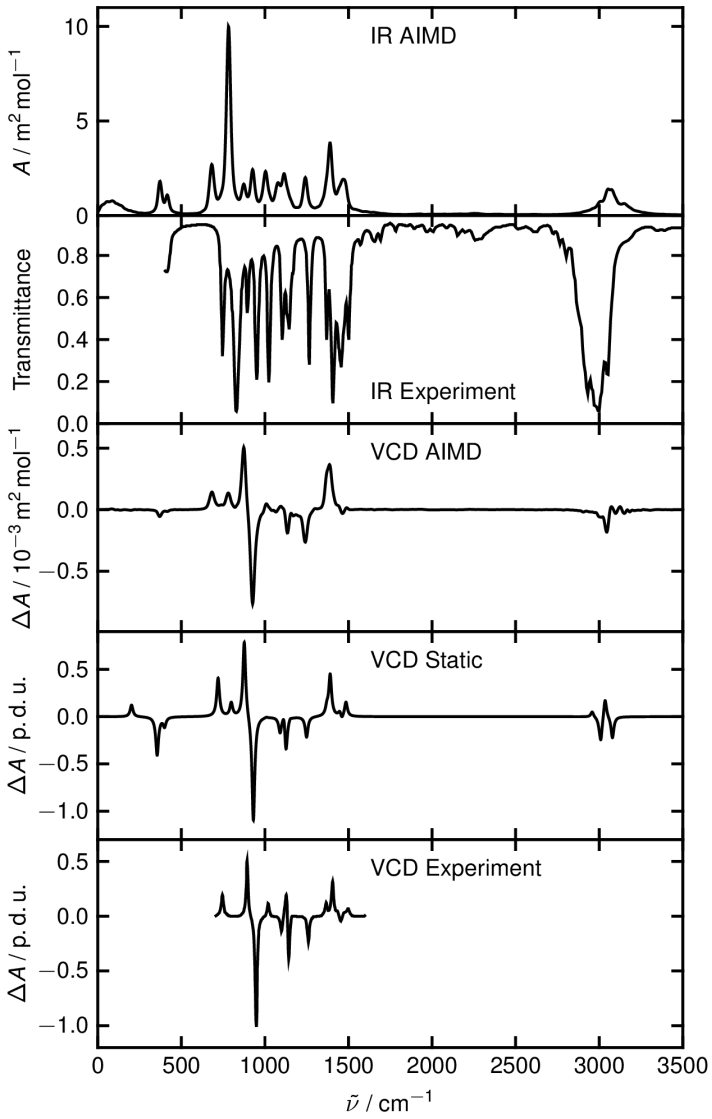

Figure S6: Simulated IR and VCD spectra of (*R*)-propylene oxide. The experimental IR spectrum is reproduced from reference 23. The experimental VCD spectrum is the inverted spectrum of the (*S*)-enantiomer reproduced from reference 24.

wavenumbers and intensities. A more accurate, but also more expensive, electronic structure method could probably reduce the deviations. Nevertheless, a combined analysis of IR and VCD spectra allows to match simulation and experiment as indicated by the dotted lines. This shows that many distinct features of the experimental VCD spectrum are reproduced very well. Considerable differences concern only the negative peak at 1265 cm^{-1} in the experiment, which is partially merged with another negative band at 1197 cm^{-1} in the simulation, the negative peak at 1063 cm^{-1} in the experiment, which is missing in the simulation, and the predicted negative band at 1143 cm^{-1}, for which no counterpart is observed in the experiment. Since the deviations are not limited to the VCD spectrum, but occur to the same extent in the IR

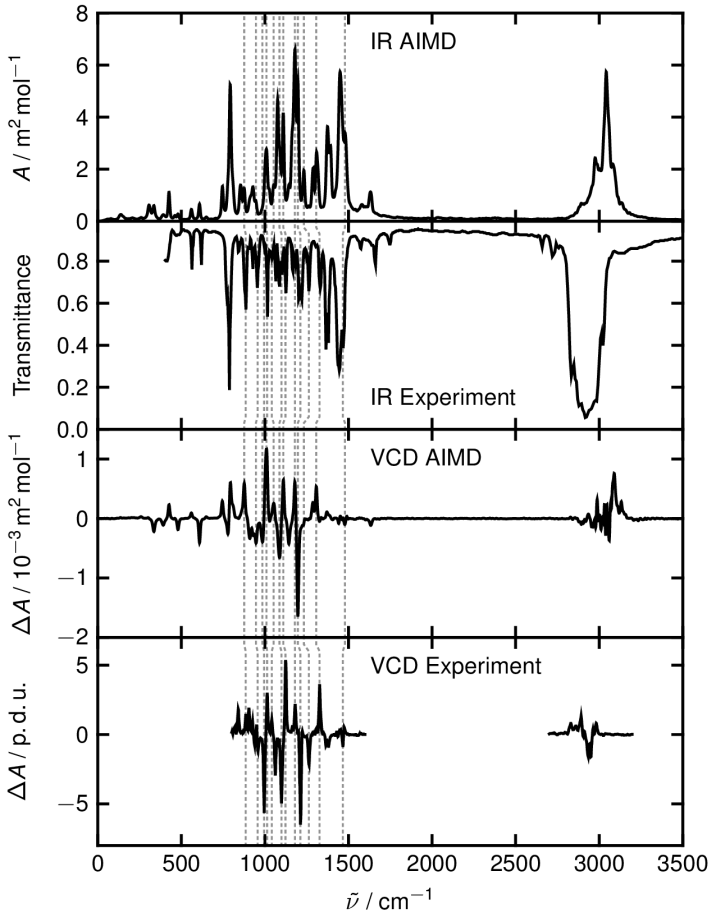

Figure S7: Simulated IR and VCD spectra of (1*R*, 5*R*)-α-pinene. The experimental IR spectrum is reproduced from reference 31. The experimental VCD spectrum is reproduced from reference 32. The dotted lines indicate the assignment between simulation and experiment.

spectrum, they are unlikely to be a primary issue of our VCD model. It is important to note that the calculated spectra would clearly be sufficient to identify the correct enantiomer of α-pinene, so the combination of experiment and AIMD could readily be used to determine the absolute configuration of the molecule.

References

[1] VandeVondele, J.; Krack, M.; Mohamed, F.; Parrinello, M.; Chassaing, T.; Hutter, J. *Comput. Phys. Commun.* **2005**, *167*, 103–128.

[2] Hutter, J.; Iannuzzi, M.; Schiffmann, F.; VandeVondele, J. *WIREs Comput. Mol. Sci.* **2014**, *4*, 15–25, see also `http://www.cp2k.org`.

[3] Becke, A. D. *Phys. Rev. A* **1988**, *38*, 3098–3100.

[4] Lee, C.; Yang, W.; Parr, R. G. *Phys. Rev. B* **1988**, *37*, 785–789.

[5] Grimme, S.; Antony, J.; Ehrlich, S.; Krieg, H. *J. Chem. Phys.* **2010**, *132*, 154104.

[6] VandeVondele, J.; Hutter, J. *J. Chem. Phys.* **2007**, *127*, 114105.

[7] Goedecker, S.; Teter, M.; Hutter, J. *Phys. Rev. B* **1996**, *54*, 1703–1710.

[8] Hartwigsen, C.; Goedecker, S.; Hutter, J. *Phys. Rev. B* **1998**, *58*, 3641–3662.

[9] Krack, M. *Theor. Chem. Acc.* **2005**, *114*, 145–152.

[10] Nosé, S. *J. Chem. Phys.* **1984**, *81*, 511–519.

[11] Nosé, S. *Mol. Phys.* **1984**, *52*, 255–268.

[12] Martyna, G. J.; Klein, M. L.; Tuckerman, M. *J. Chem. Phys.* **1992**, *97*, 2635–2643.

[13] Plimpton, S. *J. Comput. Phys.* **1995**, *117*, 1 – 19, see also `http://lammps.sandia.gov`.

[14] Wang, J.; Wolf, R. M.; Caldwell, J. W.; Kollman, P. A.; Case, D. A. *J. Comput. Chem.* **2004**, *25*, 1157–1174.

[15] Singh, U. C.; Kollman, P. A. *J. Comput. Chem.* **1984**, *5*, 129–145.

[16] Brehm, M.; Kirchner, B. *J. Chem. Inf. Model.* **2011**, *51*, 2007–2023.

[17] Thomas, M.; Brehm, M.; Fligg, R.; Vöhringer, P.; Kirchner, B. *Phys. Chem. Chem. Phys.* **2013**, *15*, 6608–6622.

[18] Thomas, M.; Brehm, M.; Hollóczki, O.; Kelemen, Z.; Nyulászi, L.; Pasinszki, T.; Kirchner, B. *J. Chem. Phys.* **2014**, *141*, 024510.

[19] Thomas, M.; Brehm, M.; Kirchner, B. *Phys. Chem. Chem. Phys.* **2015**, *17*, 3207–3213.

[20] Botchev, M.; Fokkema, D. `http://www.staff.science.uu.nl/~vorst102/software.html`, accessed November 7, 2014.

[21] Meijerink, J. A.; van der Vorst, H. A. *Math. Comp.* **1977**, *31*, 148–162.

[22] Barrett, R.; Berry, M.; Chan, T.; Demmel, J.; Donato, J.; Dongarra, J.; Eijkhout, V.; Pozo, R.; Romine, C.; van der Vorst, H. *Templates for the Solution of Linear Systems: Building Blocks for Iterative Methods*; Society for Industrial and Applied Mathematics, 1994; Electronic version: `http://www.netlib.org/templates/templates.pdf`, accessed September 12, 2014.

[23] SDBSWeb: `http://sdbs.riodb.aist.go.jp` (National Institute of Advanced Industrial Science and Technology), accessed August 10, 2015.

[24] Kawiecki, R.; Devlin, F.; Stephens, P.; Amos, R.; Handy, N. *Chem. Phys. Lett.* **1988**, *145*, 411–417.

[25] Losada, M.; Nguyen, P.; Xu, Y. *J. Phys. Chem. A* **2008**, *112*, 5621–5627.

[26] Aidas, K. et al. *WIREs Comput. Mol. Sci.* **2014**, *4*, 269–284.

[27] Dalton, a molecular electronic structure program, Release Dalton2016.0 (2015), see `http://daltonprogram.org`.

[28] Bak, K. L.; Jørgensen, P.; Helgaker, T.; Ruud, K.; Jensen, H. J. A. *J. Chem. Phys.* **1993**, *98*, 8873–8887.

[29] Weigend, F.; Ahlrichs, R. *Phys. Chem. Chem. Phys.* **2005**, *7*, 3297–3305.

[30] Luber, S.; Iannuzzi, M.; Hutter, J. *J. Chem. Phys.* **2014**, *141*, 094503.

[31] SDBSWeb: `http://sdbs.riodb.aist.go.jp` (National Institute of Advanced Industrial Science and Technology), accessed July 28, 2015.

[32] Guo, C.; Shah, R. D.; Dukor, R. K.; Freedman, T. B.; Cao, X.; Nafie, L. A. *Vib. Spectrosc.* **2006**, *42*, 254–272.